Advanced detection systems for X-ray fluorescence excitation spectroscopy

**J. Goulon,[a]* A. Rogalev,[a] G. Goujon,[a] Ch. Gauthier,[a] E. Moguiline,[a]‡ A. Solé,[a]
S. Feite,[a] F. Wilhelm,[a] N. Jaouen,[a] Ch. Goulon-Ginet,[a,b] P. Dressler,[c] P. Rohr,[c]¶
M.-O. Lampert[c] and R. Henck[c]**

[a]European Synchrotron Radiation Facility, BP 220, F-38043 Grenoble, France, [b]Faculté de
Pharmacie, Université J. Fourier, F-38700 La Tronche, France, and [c]Eurisys Mesures, BP 311,
F-67834 Lingolsheim, France. E-mail: goulon@esrf.fr

This paper accounts for selected detector developments carried out over the past 15 years within the ESRF X-ray Absorption Spectroscopy group. This includes various types of photodiodes used as integrated current detectors. Special emphasis is put on the long-standing development of a Si drift-diode array suitable for energy-dispersive detection of X-ray fluorescence. This detector, which is now operational, was used to record high-quality XMCD/ XAFS spectra on [$Fe_{70}Pt_{30}$] nanoparticles highly dispersed on a Si wafer. Using numerically deconvoluted spectra, energy resolution was decreased to 82 eV for the Si $K\alpha\beta$ line, 126 eV for the Fe $K\alpha$ line and 176 eV for the Pt $L\alpha$ line. A high-vacuum-compatible high-energy-resolution crystal analyzer was also installed on ID12, making it possible to record X-ray fluorescence excitation spectra in the photon-in/photon-out mode over a wide spectral range. Prospects of adapting these methods in order to investigate biological samples are briefly discussed.

Keywords: X-ray absorption spectroscopy; X-ray detectors; silicon drift-diodes; digital filtering.

1. ESRF beamline ID12

The ESRF beamline ID12 is dedicated to polarization-dependent X-ray excitation or emission spectroscopies without any reference to the investigation of biological materials (Goulon *et al.*, 1998; Rogalev *et al.*, 2001). Nevertheless, this beamline has been used during the construction phase of the ESRF as a test-bench for advanced instrumentation in X-ray absorption spectroscopy (XAS). This is because accurate measurements in the fluorescence excitation mode of small differential effects such as X-ray natural circular dichroism (XNCD) or X-ray magnetic circular dichroism (XMCD) spectra are extremely demanding from the quality of the whole instrumentation. The experience gained with a successful operation of ID12 has already influenced the design of other beamlines such as the ESRF beamline ID26 dedicated to XAS studies on diluted biological or geological samples (Gauthier *et al.*, 1999).

The main peculiarity of beamline ID12 is that its source is made of a sequence of three helical undulators which offer a full control of the polarization state of the emitted X-ray photons. Each undulator was specified in order to maximize the spectral range of the beamline which extends from 1.5 up to 20 keV. Helical undulators have the attractive advantage that no odd harmonics are emitted on axis: not only does this improve the spectral purity of the X-ray beam downstream to the Bragg monochromator but it also reduces the critical heat load on the first optical component of the beamline. Regarding XAS, high-brilliance undulators suffer from the major handicap that the spectral bandwidth of odd harmonics is well below 100 eV which makes such a source, *a priori*, unsuitable for extended X-ray absorption fine-structures (EXAFS) scans. Beamline ID12 was the first beamline where a micro-step gap-scan technique was successfully used to record high-quality EXAFS spectra over an energy range in excess of 1.5 keV (Rogalev *et al.*, 1998). This technique consists of optimizing the magnetic gap of the undulator during a scan of the monochromator in such a way that the energy of the monochromatic photons always matches the peak intensity of the undulator spectrum. Even though the concept may now look trivial, one should not underestimate the underlying difficulties: the average position of the electron beam in the insertion device (ID) should remain unperturbed while changing the magnetic field, and small residual perturbations, if any, should not affect the quality of the measurements.

The concept of the beamline is sketched in Fig. 1. The major optical components of the beamline have already been described in detail elsewhere (Goulon *et al.*, 1998; Rogalev *et*

---

‡ Now left the ESRF.
¶ Now with TRIXELL-THALES.

bioXAS and metallogenomics
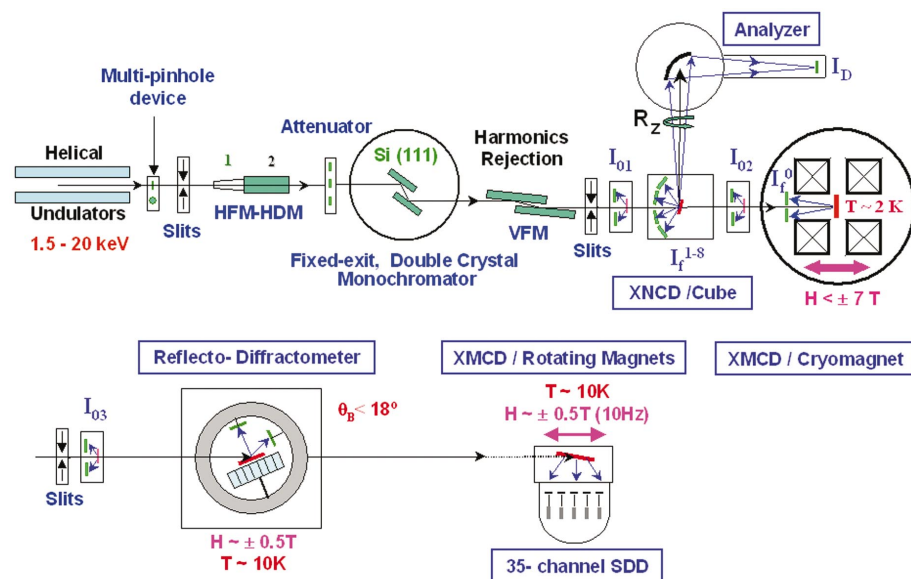
Figure 1
Block diagram of the ESRF ID12 beamline. Abbreviations: HFM-HDM, horizontally focusing and deflecting mirrors; VFM, vertically focusing mirror; I_0, beam-intensity (position) monitor; XNCD, X-ray natural circular dichroism; XMCD, X-ray magnetic circular dichroism.

al., 2001). Here, we introduce a number of experimental stations that recently became accessible to the users. Most spectra are recorded in the total fluorescence yield excitation mode using PNN^+ photodiodes formerly manufactured for us by Eurisys-Mesures. Recently, we have completed the long-standing commissioning of a 35-element array of Si drift-diodes (SDD) which have the capability to resolve several fluorescence lines and discriminate them against the scattered intensity. This detector is equipped with new digital readout/filtering electronics which look attractive for refined on-line digital processing. Finally, a high-vacuum-compatible optical analyzer equipped with spherically bent crystals has now been permanently installed in the experimental hutch: this instrument, which has the unusual capability of analyzing the polarization state of fluorescence photons, can be used to record high-resolution photon-in/photon-out resonant inelastic X-ray scattering (RIXS) spectra. This instrument opens the door to new types of valence-, spin- and site-selective XAS measurements which cannot be envisaged with energy-dispersive semiconductor detectors that have a limited energy resolution.

In the present paper, we shall concentrate on a presentation of some key technical aspects of the detection of X-ray fluorescence excitation spectra using either solid-state detectors or the crystal analyzer. Since the sensitivity and linearity of the beam intensity and position monitors developed in-house proved to be critical, especially for gap scans, we propose to start §2 with a quick description of these detectors routinely used since 1996. As a useful preamble to §3, we feel it useful to recall the considerations which led us to develop Si drift-diodes at the ESRF before we report on the commissioning tests of the 35-element SDD array at ID12. Finally, in §4 we shall give a few illustrations of what can be expected from experiments carried out with a crystal analyzer.

2. Si diodes as integrated current detectors

2.1. Beam intensity and position monitors

Silicon photodiodes operated either in photovoltaic or photoconductive modes (Knoll, 1989) offer well recognized advantages over ion chambers, especially for a windowless UHV beamline such as ID12 that is frequently operated at energies near 2.0 keV, i.e. much below the sulfur and chlorine K edges (Retournard et al., 1986; Goulon, 1991). Nevertheless, it is far from trivial to design high-sensitivity intensity monitors (I_0) featuring low insertion losses with photodiodes. Previous attempts to use amorphous silicon or CVD diamond thin films (Bergonzo et al., 1999) failed because the measured linearity of such detectors (unfortunately) did not match (yet) the highly demanding linearity criteria of XAS. To date, the most reliable option still remains to detect the X-ray fluorescence or scattered emission of a thin metal foil. The price to be paid is a loss in the detection efficiency which is not due to the photodiode itself but to the poor fluorescence yield and the restricted solid angle in which photons are collected. Such a loss of efficiency is, according to our experience, perfectly tolerable with undulator sources at third-generation synchrotron radiation facilities. Initially, the fluorescence (or scattered) photons were collected at $90°$ with respect to the direction of the incident beam (Gauthier et al., 1995; Moguiline, 1996). This detection geometry was rapidly abandoned owing to the sensitivity of the collection solid angle to the 'beam geometry', in which we include undesirable changes during a scan of the beam size, of the anisotropy of photon energy distribution, as well as small beam displacements (e.g. 20 μm or more if the monochromator is not properly set up). In 1996, all I_0 beam monitors were systematically removed and replaced by more compact devices in which the fluorescence photons back-radiated (scattered) by a metal foil or a silicium nitride film are detected using a photodiode which allows the incident X-ray beam to pass through a central hole of appropriate geometry: photodiodes with either a central circular hole (diameter 3.0 mm) or a linear slot (3.0 mm × 16.5 mm) were designed in collaboration with Eurisys-Mesures and have been routinely used for several years on the ESRF beamlines ID12, ID08 and ID26. Since the absorbing foil is now set normal to the incident beam, absorption losses are minimized whereas the distance to the diode can be adjusted in order to maximize the collection solid angle and the detection sensitivity. Moreover, the high symmetry of these detectors makes them remarkably insensitive to small changes in the beam geometry. This development immediately resulted in a major improvement of the quality of the XMCD

spectra recorded on beamline ID12. Under standard operation, typical currents delivered by I_0 monitors located downstream with respect to the monochromator are of the order of a few 10^{-6}–10^{-7} A. Such currents are easily measured using very low noise readout electronics optimized to preserve a dynamic range truly in excess of six orders of magnitude. Noise rejection performances have already been reported elsewhere (Gauthier *et al.*, 1995). Electrometers specifically designed according to our criteria are manufactured by Novelec SA in the Grenoble area. It is worth noting that the output stage of each electrometer (kept as close as possible to the detector) includes a fast voltage-to-frequency converter operated from 1 to 10 MHz with ≤ 70 p.p.m. non-linearity. Optical fibers link the electrometer to a gated digital lock-in. Its function is to minimize the whole detector electronic noise by exploiting the low-frequency modulation (at typically $F = 67$ Hz) of the fluorescence signal which is synchronous to a square-wave modulation of the incident X-ray beam caused by a mechanical chopper. A two-channel digital lock-in VME board (referenced as VDL) has been designed in-house for XAS applications (Gauthier *et al.*, 1995): since 1994, VDL boards were successfully used by several ESRF beamlines.

From the beginning it was quite obvious to us that our I_0 monitors could be operated as well as beam-position monitors using a four-quadrant photodiode still preserving the existence of the central hole. The geometrical set-up is then strictly the same as for a conventional I_0 monitor, except that the photodiode has now four independent collecting anodes associated with each quadrant diode, labelled hereafter I_j with $j = 1$–4. Whereas the total intensity $I_1 + I_2 + I_3 + I_4$ is, from symmetry considerations, still insensitive to beam instabilities (as for a standard I_0 monitor), in contrast, each individual quadrant diode I_j exhibits a marked sensitivity to small beam displacements which cause a change of the solid angle in which the fluorescence photons are collected. A barycentric location of the beam can then be deduced from the simple relations (Moguiline, 1996)

$$x_B = \frac{(I_1 + I_2) - (I_3 + I_4)}{[I_1 + I_2 + I_3 + I_4]},$$

$$y_B = \frac{(I_2 + I_3) - (I_1 + I_4)}{[I_1 + I_2 + I_3 + I_4]}.$$

Indeed, the sensitivity of this device to small beam displacements will depend on the signal-to-noise ratio of each individual quadrant channel and, implicitly, on the total integrated intensity. Recall that a dynamic range $\geq 10^6$ is typically needed in order to achieve a spatial resolution of 1 μm (Gauthier *et al.*, 1995; Moguiline, 1996). Using a calibration chart, we checked that such beam-position monitors had a vertical or lateral resolution which was of the order of 1–2 μm, at least under normal operating conditions of beamline ID12. In practice, the beam intensity and position monitors are hosted in the same UHV-compatible vessel shown in Fig. 2(*a*). A linear translator is used to insert (remove) the photodiode into (out of) the beam without breaking the vacuum; another translator at 90°

allows the users to select which metal foil or scattering film is to be used for a given experiment. Indeed, much attention was paid to the homogeneity of the films or to the thickness uniformity of the metal foils. Most frequently used are a 4 μm Ti foil and a silicon nitride (Si_3N_4) membrane (size 3.0 mm × 3.0 mm; thickness 500 nm) for experiments at very low excitation energies (Fig. 2*a*).

A critical test to evaluate the performances of I_0 monitors is the cancellation of all Bragg glitches of the monochromator on scanning EXAFS spectra in the X-ray fluorescence excitation mode (Moguiline, 1996). As another remarkable test, Fig. 3(*a*) reproduces the measured overall stability of the exit beam from the monochromator during a wide-band gap-scan of the second harmonics of the helical undulator Helios-II. Recall that the second harmonics being emitted off-axis are rather weak compared with the fundamental but benefit from a wider spectral bandwidth extending over several hundreds of eV: unexperienced users may think that this is enough to record (short) EXAFS spectra without changing the undulator gap. Unfortunately, in such a fixed gap scan, the signal-to-noise ratio will suffer from the strong variations of the incident intensity I_0 and the overall quality of the corresponding EXAFS spectra is usually rather poor. In the gap-scan technique, the intensity of the incident X-ray beam is systematically maximized and the EXAFS oscillations can be extracted with a far better signal-to-noise ratio. The difficulty, however, is to make sure that the position and the direction of emission of the X-ray beam are not significantly affected by the change of undulator gap. This is what we wish to establish with Fig. 3(*a*), which shows that the beam position does not vary significantly within ± 2.5 μm. For this test experiment we used a four-quadrant beam-position monitor which was located at 4.5 m downstream with respect to the monochromator. Unfortunately, the sensitivity of such measurements is far from sufficient to detect small angular instabilities of the source which proved to be particularly critical in X-ray dichroism measurements.

2.2. X-ray fluorescence excitation spectra

Whereas the active area of standard photodiodes is (preferably) restricted to a few cm^2 (*e.g.* 3 cm^2 for the

(*a*)   (*b*)
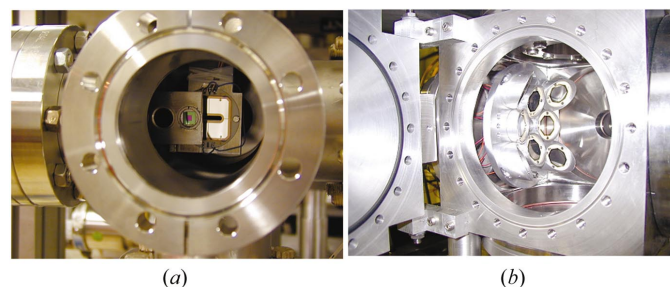
Figure 2
(*a*) Photograph of a beam-intensity (position) monitor. A clipped Si_3N_4 membrane is well apparent whereas the translator was slightly moved away in order to show two quadrants of the diode with its (oblong) hole. (*b*) Photograph of the eight-element photodiode array used for XNCD.
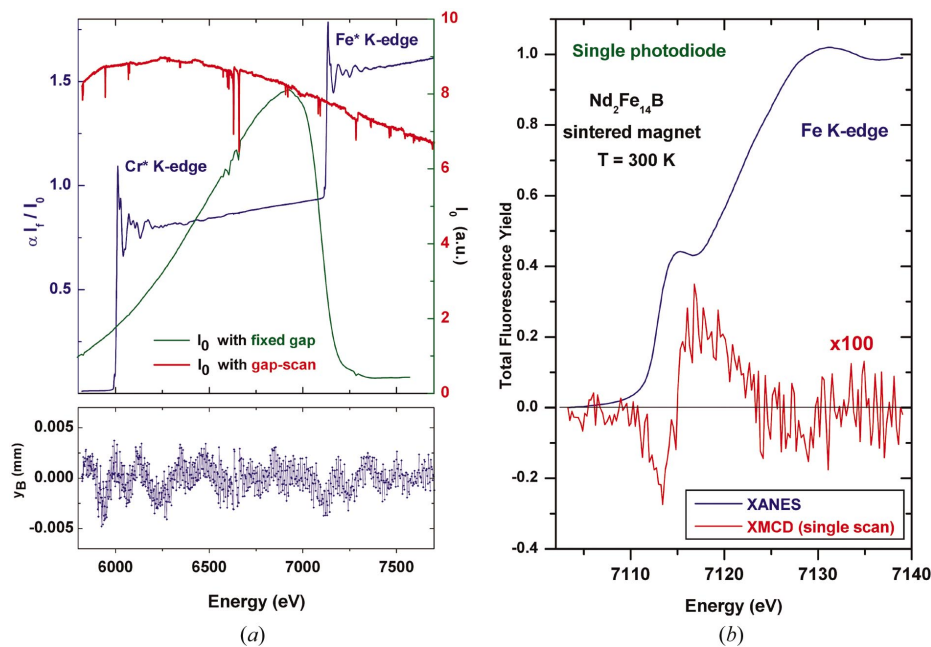
Figure 3
(a) Overall stability (y_B) of the exit beam of the monochromator measured with a four-quadrant beam-position monitor during a wide-band gap-scan; the intensity of the incident X-ray beam (I_0) was obtained by summing up the contributions of all four quadrant diodes and is displayed for reference. Bragg glitches cancel out perfectly in the fluorescence excitation spectrum $\alpha I_f/I_0$ of a test sample (magnetic tape). This spectrum was not renormalized to remove the prefactor α taking into account the different amplification gains of the I_f and I_0 detectors. (b) Single-scan XANES and XMCD spectra recorded with fast electronics detecting the high-frequency time structure of the X-ray beam at 5.68 MHz in the 16-bunch filling mode.

photodiodes manufactured by Eurisys-Mesures), we found it possible to record high-quality X-ray fluorescence excitation spectra using a multi-element array of standard photodiodes. Starting with beamline ID12, we inserted in 1996 an eight-element array into a cube-shaped vacuum vessel shown in Fig. 2(b). Similarly, a 12-element array was recently installed on the ESRF beamline ID26 for XAFS studies on dilute samples. Each diode is mounted on individual holders arranged to form a spherical array; each diode can accommodate its own individual filter assembly if one wishes to reduce the scattering background. Note that the fluorescence is detected again in the back-radiated (scattered) geometry which is most convenient for dichroism experiments: static electric or magnetic fields can be easily applied along the beam direction whereas a rotation of the sample around the beam axis also proved itself to be very useful for linear dichroism studies in mineralogy (Gaudry et al., 2003) as well as for XNCD studies on biaxial crystals (Goulon et al., 1999).

Since photodiodes are insensitive to strong magnetic fields (Knoll, 1989), we found it most convenient to insert two photodiodes directly inside the high-vacuum chamber of a 7 T cryomagnet (Oxford Instruments): (i) the first one (I_f^0) has again a central hole (diameter: 3 mm) and collects the back-radiated fluorescence just like the previously described I_0 monitors; (ii) the second diode (not sketched in Fig. 1) collects the fluorescence at 90° from the incident beam in a more classical geometry. This chamber is routinely used for XMCD measurements, including difficult experiments on

paramagnetic systems or on thin-film multilayers in the hard X-ray range.

Recently, we developed the capability to record high-resolution X-ray absorption near-edge structure (XANES) spectra simultaneously from two different samples located in the 'cube' and in the cryomagnet, respectively. This required the insertion of an additional I_0 monitor between the two sample chambers (i.e. I_{02} in Fig. 1). Given the excellent linearity properties of our beam-intensity monitors, there is no detectable contamination of the XANES spectrum of the downstream sample owing to the absorption by the sample located upstream. High-quality drift-free difference XANES or EXAFS spectra can thus be recorded in this way. Even more important, if the first sample does not exhibit any dichroism, we can use the corresponding XANES spectra to detect and very accurately monitor any eventual angular drift of the machine over consecutive scans or after a refilling of the storage ring. After proper correction, angular instabilities can be kept below 0.05 µrad over several days. This proved to be absolutely essential to avoid the contamination of weak dichroism signals by derivative-like artefacts.

The latter development greatly benefitted from a recent upgrade of the VDL boards: the newly commissioned FIDL boards (which are now operated in a compact PCI environment) combine in a single device up to 12 lock-in channels all perfectly synchronized. The FIDL boards also offer further advantages: (i) the raw data are now stored in on-board SDRAM with local pre-processing capabilities; (ii) each channel can accommodate a 'double modulation' which is highly attractive for dichroism experiments exploiting AC modulation techniques; (iii) modulation frequencies as high as 50 kHz can be exploited, e.g. for circularly polarized X-ray excited optical luminescence (XEOL) applications. In parallel, much time and effort were invested in a new design of high-speed electrometers. In order to give a flavour of what was already achieved, we have reproduced in Fig. 3(b) single-scan XANES/XMCD spectra recorded at a modulation frequency of 5.68 MHz, i.e. the bunch repetition frequency in the 16-bunch filling mode of the ESRF storage ring. Indeed, no mechanical chopper is needed anymore and the detection cyclic ratio is maximized. Moreover, the analogue lock-in operated at 5.68 MHz could benefit from a jitter-free reference signal directly available from the RF master clock. We expect such developments to open a completely new field of applications for X-ray dichroism at intermediate frequencies (IF) and, possibly, at radio frequencies (RF).

Regarding BioXAS, we wish to stress the time-resolved experiments carried out at much longer time scales in the 'quick gap-scan' mode pioneered by Solé *et al.* at the ESRF beamline ID26. Using a multi-element photodiode array, it was demonstrated that within a short data-acquisition time (Δt = 2.95 s) high-quality iron K-edge XANES spectra could be recorded from a solution of carbonmonoxymyoglobin (concentration 7 mMol l^{-1}). Similarly, a 1000 data point EXAFS spectrum extending over 1 keV was recorded in Δt = 10 s using the same solution (Solé *et al.*, 1999). This is particularly exciting for biological samples or catalysts which very often suffer from dramatic radiation damage over long data-acquisition times. This experiment would have been just impossible with any count-rate-limited energy-dispersive detector.

3. Si drift-diodes as energy-dispersive detectors

It has long been known that a large scattering background or a strong matrix fluorescence signal can cause a dramatic degradation of the signal-to-noise ratio (S/N) in XAS spectra,

$$\mathrm{S/N} = \left[N^F \Delta t / (1 + A) \right]^{1/2},$$

where Δt is the data-acquisition time and $A = [N^B/N^F]$, with N^F and N^B referring to the fluorescence and background count rates, respectively. One might think of simply increasing either the incident flux and N^F, or the data-collection time Δt but this would not be a good choice at third-generation synchrotron radiation facilities where the probability of radiation damages is quite high, especially for BioXAS studies. It is preferable to remove the unwanted background by discriminating the energy E^F of the fluorescence photons. As discussed in §4, a Bragg crystal analyzer, which offers a high energy resolution at the expense of a very restricted angular acceptance, can be a valuable alternative option. In the present section, we shall first consider the use of multi-element energy-dispersive solid-state detectors which offer a higher count rate but with a rather poor energy-resolving power.

3.1. A concept minimizing the electronic readout noise

At low excitation energy (*i.e.* below 5 keV), energy discrimination is not trivial because the energy difference $\Delta E = [E^B - E^F]$ is approaching the semiconductor intrinsic noise, $\Delta E_{\mathrm{intr}} = 2.35[FE^F \delta E_{\mathrm{eh}}]^{1/2}$, where F is the Fano statistical parameter and δE_{eh} is the energy required to create one electron–hole pair. Actually, the energy resolution is even worse owing to additional noise sources which include the readout electronic noise ΔE_{read} and collection losses ΔE_{coll} so that

$$\left[\Delta E_{\mathrm{FWHM}}\right]^2 = \left[\Delta E_{\mathrm{int}}\right]^2 + \left[\Delta E_{\mathrm{read}}\right]^2 + \left[\Delta E_{\mathrm{coll}}\right]^2.$$

There is surely nothing we can do against the intrinsic noise, but we wish to show below that Si drift-diodes minimize the electronic readout noise which is becoming a major source of energy dispersion below 10 keV, as proved by Fig. 4(*b*).

On the other hand, the detector electronics are expected to have a non-linear response to the input count rate N_i. The throughput rate N_o is given by

$$N_o = N_i \exp(-N_i \tau_{\mathrm{D}}) \left[1 - \frac{N_i G \bar{E}}{(\mathrm{DNR}/T_{\mathrm{res}}) - N_i G \bar{E}} \right].$$

The first term is the well known throughput rate of paralyzable electronics characterized by the dead time τ_{D} (Knoll, 1989). The second term is a correction due to the reset dead time which becomes quite significant at high count rates. Here, G is the event gain at the preamplifier output, $\bar{E}$ the average energy of the input spectrum, DNR the dynamic range of the preamplifier and T_{res} is the reset dead time of the charge preamplifier (see, for instance, Farrow *et al.*, 1998). With a triangular pulse shaper, τ_{D} is equal to the total processing time 2τ where τ denotes the so-called peaking time. As illustrated in Fig. 4(*a*), there is ~63% loss at the maximum count rate, but, what is even more a concern for EXAFS, the slope vanishes, which means that the detection system has no differential sensitivity and cannot detect small variations in the measured fluorescence yield. Thus, it is mandatory to

(*a*)

(*b*)

(*c*)

(*d*)
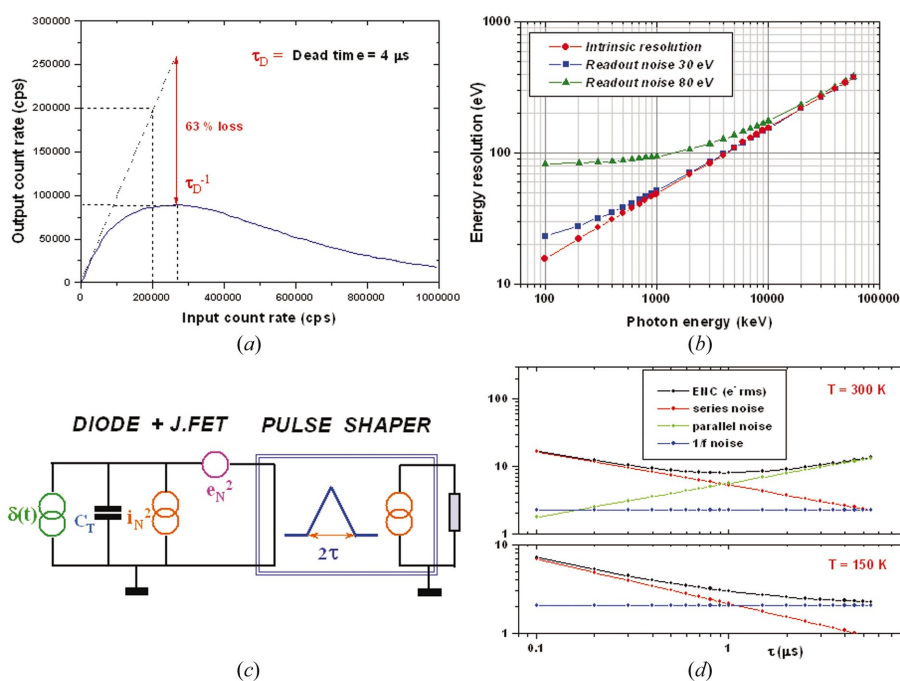
Figure 4
Basic concepts for the readout electronics of Si drift-diodes. (*a*) Throughput rate in a paralyzable detector. (*b*) Degradation of the energy resolution owing to intrinsic and readout noises. (*c*) Electronic scheme including series and parallel noise sources. (*d*) Contribution of various noise sources to ENC as a function of the peaking time.

minimize the processing time to operate such a detector at a synchrotron radiation source.

The noise properties of the readout electronics are formally described using the equivalent scheme of Fig. 4(c), in which it is a common practice to distinguish between the voltage series noise, $e_N^2 = a_w + a_f/f$, and the parallel current noise, $i_N^2 = b_w + b_f/f$. We also systematically included the $1/f$ noise components in addition to the white-noise terms. The equivalent noise charge (ENC) is defined as the stored charge for which S/N = 1. Typically,

$$\text{ENC}^2 = A_1 a_w C_T^2 (1/\tau) + A_2 \left[2\pi a_f C_T^2 + b_f/(2\pi)\right] + A_3 b_w \tau,$$

where the linear coefficients A_j are parameters that depend on the nature of the triangular or semigaussian filter used; $C_T = C_{\text{diode}} + [C_{\text{JFET}} + C_{\text{stray}}]$ denotes the total input capacitance. We have reproduced in Fig. 4(d) a simulation based on realistic parameter values (Pinotti, 1993). Since it is a rather common practice in the specialized literature to express ENC in e^- r.m.s., let us recall that ENC (eV, FWHM) = $2.35 \delta E_{\text{eh}}$ ENC (e^- r.m.s.). In any case, Fig. 4(d) shows that ENC exhibits a well defined minimum for some (optimum) peaking time which is temperature dependent: $\tau_{\text{opt}} = (A_1/A_3)^{1/2} [a_w/b_w]^{1/2} C_T$. At optimum energy resolution, one obtains

$$\text{ENC}^2_{\text{opt}} = \left(2\pi a_f A_2\right) C_T^2 + 2(A_1 A_3)^{1/2} [a_w b_w]^{1/2} C_T + A_2 \left(b_f/2\pi\right),$$

in which the quadratic dependence in the total input capacitance is quite noteworthy. Regarding XAS applications, two different regimes should be distinguished: (i) energy resolution should be maximized for XANES (XMCD) experiments carried out at low excitation energy ($E^F \leq 5$ keV) and thus operation at the optimum shaping time is highly recommended; (ii) energy resolution is rarely the critical issue for EXAFS studies and the events should be preferably processed as fast as possible. Nevertheless, under all circumstances, one should minimize C_T and favor the matching condition: $C_{\text{diode}} \simeq [C_{\text{JFET}} + C_{\text{stray}}]$. This implies that one should minimize a_w which is originating in the input J.FET, but also keep the leakage current of the diode as low as possible, since $b_w = q I_{\text{leak}}$. This is where the quality of the industrial process is critical.

The drift-diode concept introduced by E. Gatti and P. Rehak in 1984 precisely makes it possible to keep the capacitance C_{diode} small even for a diode with a large active area. This is because the electrons generated by photoabsorption in a reverse-biased Si diode are constrained by an additional electric field to drift towards a collecting anode that has a small size and therefore a small capacitance (Gatti & Rehak, 1984). This concept is illustrated in Fig. 5(a) for a cylindrical Si drift-diode in which the drift field acts on the electrons as a kind of electrostatic funnel. Such a drift field is created by biasing to appropriate potentials P^+ electrodes implanted on both sides of a high-resistivity N silicon wafer. On the back face, the electrodes are separated by thin layers (~ 2000 Å) of thermally grown SiO_2; the N^+-implanted collecting anode is also located on the back face. For simplicity, guard electrodes,

which are needed to prevent charge injection from undepleted regions, were omitted in Fig. 5(a). The first experimental demonstration of the validity of the Si drift-diode concept was produced in 1990 by Kemmer and his colleagues in München (Kemmer et al., 1990).

Reducing only C_{diode} is insufficient and, over the past decade, new types of external J.FETs have been developed. The first one, put on the market by Link Analytical, was the so-called pentafet (Nashashibi & White, 1990), which had not only a low input capacitance ($C_{\text{JFET}} = 1.2$ pF) but also an additional electrode used to reset the charge preamplifier with very little extra noise by exploiting the gate leakage current of injected holes. An upgraded version (i.e. the EuriFET) was developed by Eurisys-Mesures with a slightly lower capacitance, $C_{\text{JFET}} = 0.9$ pF. Recently, a very low capacitance J.FET ($C_{\text{JFET}} = 0.47$ pF) also became available to Canberra Semiconductor NV. Thus, over the past decade, technology has made it possible to reduce C_{JFET} by as much as one order of magnitude if one refers to the now fully outdated 2N4416 J.FET ($C_{\text{JFET}} = 4.2$ pF). The corresponding advantage is not restricted to only Si drift-diodes but also benefits high-purity germanium pixel detectors (HPGe).

Advanced technologies now make it possible to integrate the input J.FET directly on the anode of Si drift-diodes. Pioneering works in the past decade (Radeka et al., 1989; Bertuccio, Gatti et al., 1992; Pinotti et al., 1993; Sampietro, Fasoli et al., 1995; Matsuura & Nishida, 1998; Sonsky et al., 2000) resulted in the emergence of a new generation of X-ray detectors (Strüder et al., 1997, 1998). Current efforts now focus on the minimization of the reset noise: this led Sampietro and his colleagues to propose a new concept of continuous reset that should result in an improved stability and a better linearity at high count rates (Guazzoni et al., 2000; Sampietro et

(a)

(b)
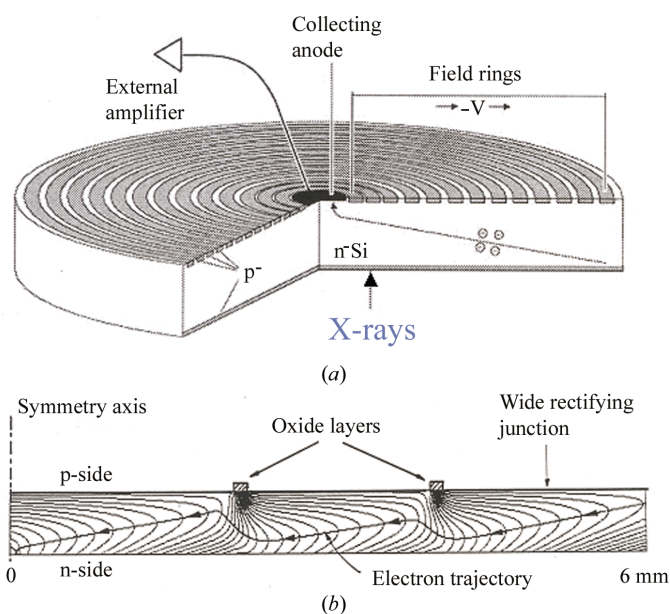
Figure 5
(a) Cylindrical Si drift-diode concept. (b) Drift field topology resulting in a so-called 'zigzag' trajectory of the electrons.

al., 2000). Even though the J.FET integration technology has apparently reached its full maturity, as reflected by recent publications (Lechner et al., 2001; Longoni et al., 2002), it still remains to be fully established that integrated J.FETs do not suffer from radiation damage after long exposure times under very intense X-ray beams produced by third-generation undulator sources. Note that the integration of the input J.FET on other semiconductor detectors (e.g. HPGe) can hardly be envisaged within the present state of technology.

3.2. Drift time related issues

Even though a Si drift-diode has an extremely low capacitance, it is not a very fast detector. This is because it takes some time $\tau_d = L/(\mu E_d)$ for the photoelectrons (represented as Dirac pulses) to drift over a pathlength L towards the sensing anode, in a drift field E_d and with the standard carrier mobility in silicon, $\mu = 1300$ cm^2 V^{-1} s^{-1}. Typically, $\tau_d \simeq 1$ µs for $L = 3$ mm in a drift field of 250 V cm^{-1}. During the drift time, there is some spread of the electron cloud, $\sigma_e(L) = [2D\tau_d]^{1/2} \simeq 82$ µm, that can be converted as well into a spread time $\tau_e \simeq 25$ ns. The collecting anode has itself a finite impulse response τ_{coll} that may be of the same order of magnitude. However, the total input pulse-broadening $\tau_{in} = (\tau_e^2 + \tau_{coll}^2)^{1/2}$ is usually found to contribute only in a marginal way to the so-called ballistic deficit in pulse height ($\sim 0.3\%$) mostly determined by the shaper. Since two coincident events can be fully resolved with a Si drift-diode if their drift times differ by more than the processing time τ_d, one may question whether the pile-up statistics are the same with a uniform pixel detector or a Si drift-diode. This problem has been recently addressed by Pietraski & Furenlid (2000), who concluded that the pile-up statistics were strictly identical for both detectors in the case of quasi-continuous X-ray sources. The time structure of synchrotron radiation sources has, however, to be carefully taken into consideration when the maximum drift time τ_{dm} and the shaping time are becoming comparable or even shorter than the bunch repetition period τ_b. At the ESRF, this may happen in the single-bunch and 4- or 16-bunch filling modes of the machine. Whenever the condition $\tau_d \leq \tau_{dm} \simeq \tau_b$ holds true, then a linear drift detector could have fewer corrupted events than a pixel detector. This is (unfortunately) not the case for drift diodes with cylindrical geometry: the latter would even suffer from a small penalty factor (0.811) in their pile-up statistics at very high count rates. The case of macro-bunches (e.g. in the 2/3 filling mode of the ESRF storage ring) would deserve more attention (Bateman, 2000).

3.3. SDD diodes devices tested at the ESRF

During the construction of the ESRF XAS beamlines, we were fascinated by the prospect of obtaining Si photodiodes with a large active area, a high counting rate and a good energy resolution. With the assistance of Gatti's collaborators at the Politecnico di Milano and with proper technological investments from Eurisys-Mesures (formerly Intertechniques), we succeeded in designing, in 1994, octagonal Si drift-diodes with an active area as large as 1 cm^2 but with a

capacitance as small as $C_{diode} = 150$ fF. With a standard 2N4416 external J.FET, the energy resolution of 143 eV (FWHM) measured at 150 K with a Fe^{55} source was found to be very promising (Gauthier et al., 1994). This work also established the value of a new electrode topology inducing a kind of 'zigzag' electron path shown schematically in Fig. 5(b) (Gauthier, 1992; Bertuccio, Castoldi et al., 1992). Its main advantage was to preserve large drift fields with a minimum amount of oxide dead layers on the front face: this is essential for the use of Si drift-diodes at low excitation energy. This concept was retained for our subsequent projects and was adopted as well by other groups (Iwanczyk et al., 1996, 1999).

Increasing the active area of the Si diodes gives more flexibility to handle the problem of complex sample environments that are frequently required in exotic XAS or XMCD experiments: very often, the detector cannot be kept very close to the sample and a large active area makes it then possible to preserve a reasonable solid angle. Count-rate consideration led us to envisage as a next step the design of multi-anode drift diodes with an active area of 2 cm^2 (Moguiline, 1996; Moguiline et al., 1997). In this detector, the collection zone was split into eight N$^+$-implanted anodes separated by P$^+$ electrodes as shown in Fig. 6(a). It was planned to assemble together four diodes of this type to

N^+

SiO$_2$

P^+

(a)

(b)
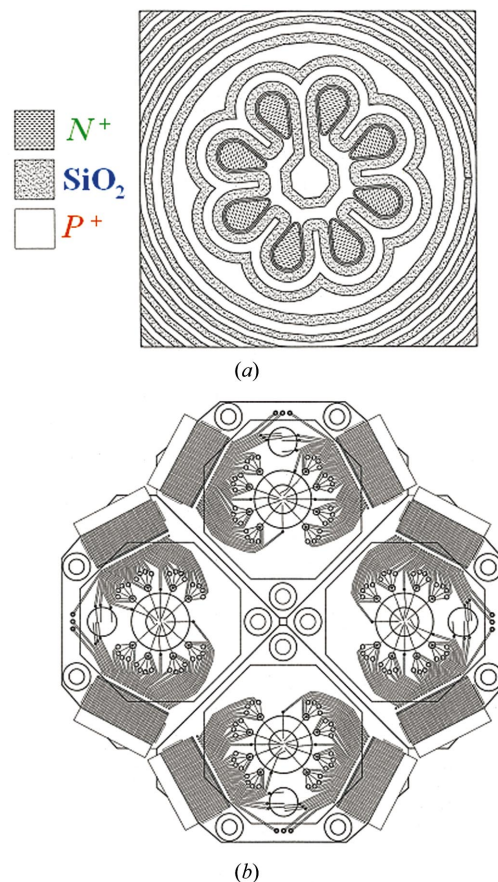
Figure 6
(a) Enlarged detail drawing of the collection zone of the ESRF prototype eight-anode Si drift-diode. (b) Back face of the ESRF prototype 32-channel drift-diode assembly. Note the huge number of connectors required to generate a very basic drift field.

produce a 32-channel detector (Fig. 6*b*) that could have been immediately used for real operation at an XAS beamline. As illustrated by Fig. 6(*b*), the complexity of the cabling problems increased rapidly and we had to minimize the number of connections required for the polarization electrodes. Unfortunately, we failed to generate the desired uniform drift-field over the whole active area and we hardly succeeded in obtaining more than 12 channels simultaneously tuned to the expected maximum count rate. The rather low peak-to-background value ($\sim$800) supported our interpretation that the charge collection was imperfect. Nevertheless, it was already a positive outcome to establish that the concept of a multi-anode drift diode should work since we did not detect any cross-talk between the anodes whereas there was no clear evidence of a serious charge-splitting problem. Although this prototype detector was far from being optimized, it could already be used to record the cobalt *K*-edge EXAFS spectrum of a highly dilute aqueous solution of cobalt acetate (concentration 200 µMol l^{-1}, *i.e.* 12 p.p.m. of Co) with only 12 active channels (see Gauthier *et al.*, 1999).

By the same time and as part of a joint EEC project, ESRF has financially contributed to the design and to the evaluation on beamline ID12 of a six-element Si drift-diode with on-chip electronics (Gauthier *et al.*, 1996, 1997; Strüder *et al.* 1997, 1998). With a sensitive area per channel of 3.5 mm^2, the total active area of the whole detector was only 21 mm^2, which is quite small in view of the solid angle required by most ESRF XAS experiments. With a shaping time as short as 0.5 µs, the FWHM energy resolution of such a six-element Si drift-diode at the Mn K_α line was 227 eV at room temperature and decreased to 152 eV at 150 K. As a typical test experiment, we have recorded with this detector the Ce L_{III}-edge EXAFS spectra of a macrocyclic complex of cerium (TETP:Ce) by selectively monitoring the intensity of the $L_{\alpha1,\alpha2}$ fluorescence lines. The EXAFS spectra were shown to be still contaminated by a weak signal anticorrelated with the Ce L_{II}-edge XANES signature, in full agreement with earlier predictions made by Goulon *et al.* (1982). Apparently, a 39-cell Si drift-detector, still with on-chip electronics, featuring a total active area of 195 mm^2, was also designed (Strüder *et al.* 1997, 1998) but, regrettably, ESRF was never offered the opportunity to investigate its performances for real XAS applications.

3.4. Analog/digital front-end

Highly compact analog front-end electronics modules with a minimized power consumption are under development for the next generation of SDD arrays that should accommodate several hundreds of channels. In this perspective, we note that a very promising VLSI processor (ROTOR) is being developed by Pullia *et al.* (Pullia *et al.*, 1998; Pullia, Fiorini *et al.*, 2000) for high-rate high-resolution spectroscopy: this patented concept should offer almost optimal impulse response filters and would minimize pile-up without requiring any fast channel to trigger the events. Note that a more conventional 16-channel ASIC for Si drift-diodes readout (ICARUS-SDD) has already been designed and was shown to have even better performances than a standard (commercial) spectroscopic chain (Labanti *et al.*, 2000).

In the initial ESRF Si drift-diode project (Goulon, 1991) we had in mind to equip up to 64 channels, and an approach based on multichannel digital pulse processing did look most attractive, not only in terms of costs but also in terms of flexibility and performances (Georgiev & Gast, 1993; Jordanov & Knoll, 1994; Sampietro, Bertuccio *et al.*, 1995; Sampietro, Geraci *et al.*, 1995; Stein *et al.*, 1996). As noted by Pullia, Geraci & Ripamonti (2000), digital pulse processing benefits from serious advantages: (i) the possibility to implement optimal filters; (ii) the insensitivity to pick-up noise after digitization; (iii) the flexibility to reconfigure or recalibrate the whole system with simple software procedures. This led us to develop in-house two low-cost multichannel digital shapers both designed in a VXI environment: the first version (*i.e.* DDA) could accommodate only three channels on a single C-sized VXI board (see Gauthier *et al.*, 1998) and was used mostly as a prototype with the eight-anode Si drift-diode detector described in §3.3; the upgraded version, XDS-2000 (Goujon *et al.*, 1998), accommodates four shaper channels on the same VXI board and was developed to operate the new 35-element drift-diode array now installed on beamline ID12. The hardware to equip up to 64 channels in this way is available. Both versions (*i.e.* DDA and XDS-2000) were adapted from an initial architecture first proposed by Bordessoule & Bosshard (1995). A simplified organigram of XDS-2000 is reproduced in Fig. 7:
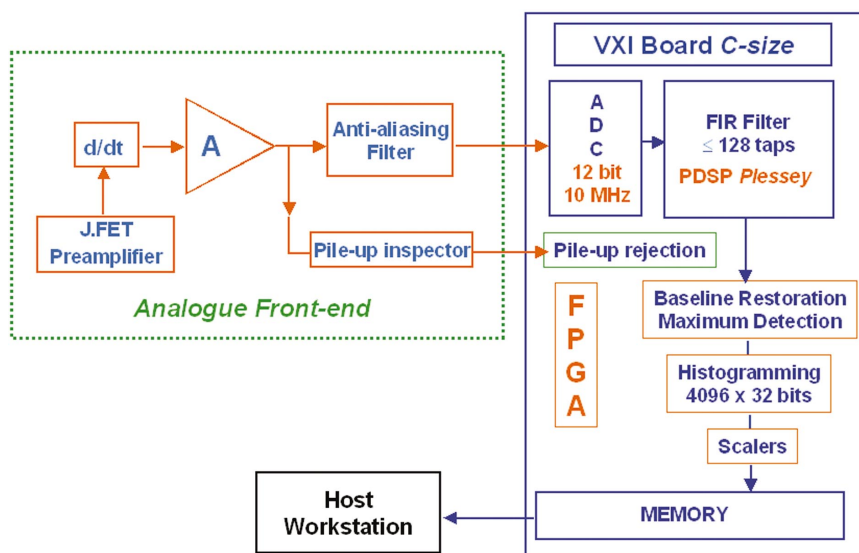
Figure 7
Block diagram of the four-channel XDS-2000 VXI board. Only one single readout channel is shown.

(i) In the slow channel, the output of the charge preamplifier is first differentiated and noise whitening is performed; a second amplifier stage which includes an anti-aliasing filter was added to benefit from the full dynamic range of the ADC. Digitization is performed with a 12-bit ADC (10 MHz). The samples are then transferred to a PDSP (Plessey) which carries out the FIR filtering with up to 128 coefficients. Any kind of filter shape can be synthesized with peaking times ranging from 500 ns to 6.4 µs.

(ii) Following a fast differentiation/amplification stage, a fast channel delivers a triggering signal used by the pile-up inspector to validate or inhibit the peak maximum detection in the slow channel. The pulse-pair resolution in the fast channel is 500 ns.

(iii) Powerful FPGAs (XILINX) are used to trigger the pile-up rejection, to restore the baseline according to various strategies, to detect the pulse maxima and to histogram the pulse heights into memory buffers which are read periodically. Further local 'on-line' pre-processing of the data has now become possible. This includes the definition of regions of interest in the spectra, count-rate integrations over given regions of interest *etc.*

For diagnostics purposes, each shaper can be rapidly reconfigured into a digital oscilloscope to display filtered (unfiltered) pulses and perform the FFT analyses. A major drawback of the design of Bordesoule & Bosshard (1995) was the absence of any digital baseline restoration. Theoretically, there is no need for a baseline restorer (Jordanov & Knoll, 1994), but it is our experience that real detectors have defects (imperfect charge collection, fluctuations of the dark current with photon flux *etc.*) which result in unwanted long tails requiring careful baseline corrections. This point was confirmed in several recent papers (Stein *et al.*, 1996; Pullia, Geraci & Ripamonti, 2000). Bipolar filters with area-balanced impulse response were proposed to remove baseline slow distortions (Ripamonti & Pullia, 1996). Typically, improper baseline corrections cause the energy of the fluorescence lines to drift and degrade the energy resolution. Such undesirable effects become most dramatic at very high count rates where any baseline restorer becomes less accurate. This is obviously of great concern for XAS applications at synchrotron radiation sources. Stand-alone DSP-based spectrometry chains have recently become commercially available (*e.g.* DXP-Saturn from XIA; InSpector 2000 from Canberra Industries) but face the same difficulties. While a peak stability of 0.1% as a function of the count rate is becoming standard, a new algorithm by XIA made it possible to reach the astounding stability of 0.02%. It is envisaged to upgrade the ESRF XDS system hardware with faster ADC

(25 MHz/16-bit) and larger FPGAs in order to further push the performances according to our needs whereas application-oriented softwares should soon become available.

3.5. Commissioning a 35-element SDD array: first results

As illustrated by Figs. 8(*a*) and 8(*b*), the ESRF SDD-2000 project is based on an array of 7×5 discrete cylindrical Si drift-diodes, each having an active area of 10 mm^2 and an anode diameter of 200 µm suitable for the operation with an external EuriFET. This rather conservative concept was preferred for user operation because we wanted the detector to be robust and radiation hard but also easy (cheap) to repair in case one pixel did not meet the expected performances. The Si drift-diodes were manufactured by Eurisys-Mesures (Lingolsheim) which also delivered the analogue preamplifier cards. The detector that is currently operated windowless at its optimum temperature ($T = 143$ K) is housed in a special UHV-compatible chamber. For the reception tests, the FWHM energy resolution of individual diodes measured with a ^{55}Fe source was as good as 129 eV using a processing time of 12 µs whereas a peak-to-background (PTB) ratio in excess of 1000 was obtained.

The first experiment carried out during the commissioning test of the detector at beamline ID12 concerned XMCD spectra recorded on [Fe$_{70}$Pt$_{30}$] nanoparticles embedded in organic polymers and dispersed on top of a Si wafer. As illustrated by Fig. 9(*a*), the average diameter of these particles was ~6 nm and their concentration was $\leq 10^{13}$ Pt atoms mm^{-2}. At such a low concentration, even the Pt L_{III} absorption edge itself was found to be hardly measurable with a standard photodiode. As shown in Fig. 9(*b*), we were able to detect at low temperature ($T = 20$ K) not only the XANES spectra but also the XMCD signals at the Pt L_{III} and L_{II} edges in a weak magnetic field of 0.4 T. The quality of the data was high enough to allow us to exploit the XMCD sum rules

Back face   Front face

(*a*)   (*b*)
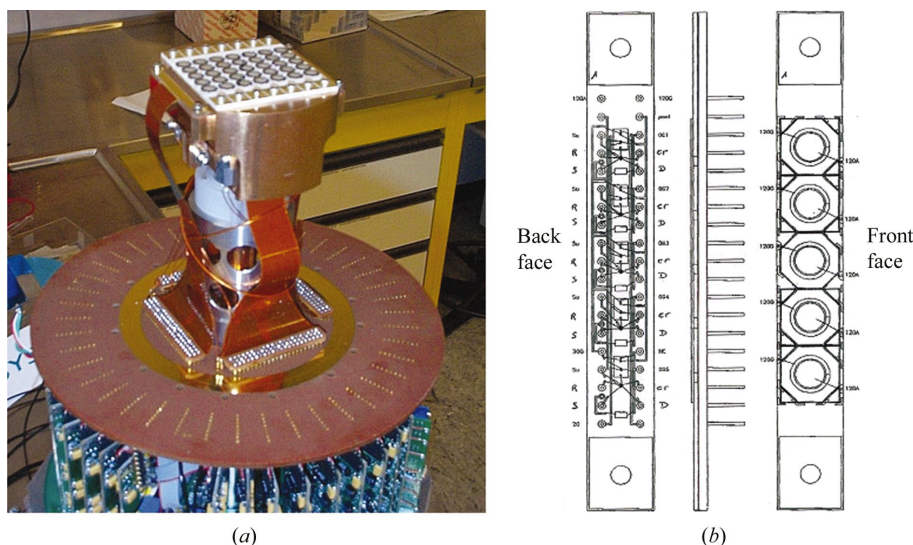
Figure 8
(*a*) Photograph of the 35-element SDD array now installed on the ESRF beamline ID12. (*b*) Details of a five-element linear array.

bioXAS and metallogenomics

(Thole *et al.*, 1992; Carra *et al.*, 1993) and to derive for the first time the local spin and orbital magnetic moments of Pt in the $5d$ states: $\langle S_z \rangle = 0.079 \, \mu_B$, $\langle L_z \rangle = 0.008 \, \mu_B$.

During these experiments, the counting rate in the $L_{\alpha 1}$ line was 20 kcounts s^{-1} channel^{-1} with a peaking time of 0.5 µs. Even though the X-ray beam was impinging on the sample with an angle of incidence of $\sim 15°$, the beam footprint was quite small: 300 µm × 30 µm. This is because we had to close down the slits in order to avoid an excessive overall count rate owing to the strong soft X-ray fluorescence signal of the Si wafer. The energy resolution of the emission spectra recorded with one single SDD channel (data acquisition time 60 s; peaking time 0.5 µs) is illustrated in Figs. 9(c) and 9(d): it was of the order of 132 eV for the unresolved Si $K_{\alpha\beta}$, 159 eV for the Fe K_α line and 202 eV for the Pt $L_{\alpha 1}$ line. However, by using a fast numerical deconvolution of these emission spectra the latter figures were easily decreased to 82 eV, 126 eV and 176 eV, respectively, at the expense of some enhancement of the noise level. Such a noise increase, however, is not dramatic in our application since we are interested in the integrated area under now well resolved peaks. Recall that numerical deconvolutions are also a common practice in γ-ray spectroscopy. Further application-oriented digital processing will allow us soon to rescale the spectra with respect to the contribution of some selected matrix fluorescence line, *e.g.* the strong Si $K_{\alpha\beta}$ line, in order to remove the count-rate non-linearities as already suggested by Pietraski *et al.* (1999).

## 4. High-resolution X-ray fluorescence excitation spectra recorded with a spherically bent crystal analyzer

There are various types of optical analyzers which fill different niches in the XAS toolbox. Multilayer mirror analyzers (Zhang *et al.*, 1998, 1999) are best used for recording EXAFS spectra of dilute samples at rather low emission and excitation energies, *i.e.* only when the Bragg angle is large enough to preserve a reasonable energy resolution as well as a wide angular acceptance. In contrast, bent Laue crystal analyzers, which benefit from a wide angular acceptance and low insertion losses at high energy (Zhong *et al.*, 1999), have been successfully used to resolve close-lying fluorescence lines of actinides.

In the present section, we wish to stress the complementarity of the spectroscopic information that can be obtained with high-resolution Bragg-type analyzers operated in the most simple Johann geometry. A photograph of the instrument installed on the ESRF beamline ID12 is reproduced in Fig. 10(a). Resonant inelastic X-ray scattering (RIXS) or fluorescence photons emitted along the vertical axis **z** are analyzed by Si crystals (100 mm in diameter) spherically bent to a fixed curvature radius $R = 1$ m defining the diameter of the Rowland circle on which the sample source point and the detector are both located. The diffraction plane is vertical but can be freely rotated around the **z** axis for polarization analyses of the emitted X-ray photons. The energy resolution of this analyzer benefits from the small vertical focus size of the incident beam (~ 30 µm) used to excite the sample. The Johann geometry suffers from an extra aberration term with respect to the Johannson geometry, but this term becomes very small at large Bragg angles ($\theta_B \geq 45°$) if both the source and detector are truly located on the Rowland circle (Matsushita & Hashizume, 1983). Note that the instrument installed on ID12 is high-vacuum compatible and can thus be operated at low emission/excitation energies using appropriate crystals. We have compared in Fig. 10(c) the normalized XANES spectra of a single crystal of ZnO (Würtzite-type structure, $P6_3mc$) recorded simultaneously with our eight-photodiode array and with the crystal analyzer. In this experiment (Fig. 10b), a diamond quarter-wave plate (QWP) was used to convert the incident circularly polarized X-ray beam into (σ) or (π) linearly polarized components with the capability to flip rapidly the polarization direction. The (001) ZnO crystal was slightly inclined ($\varphi \simeq 5°$) in order to analyze the emitted
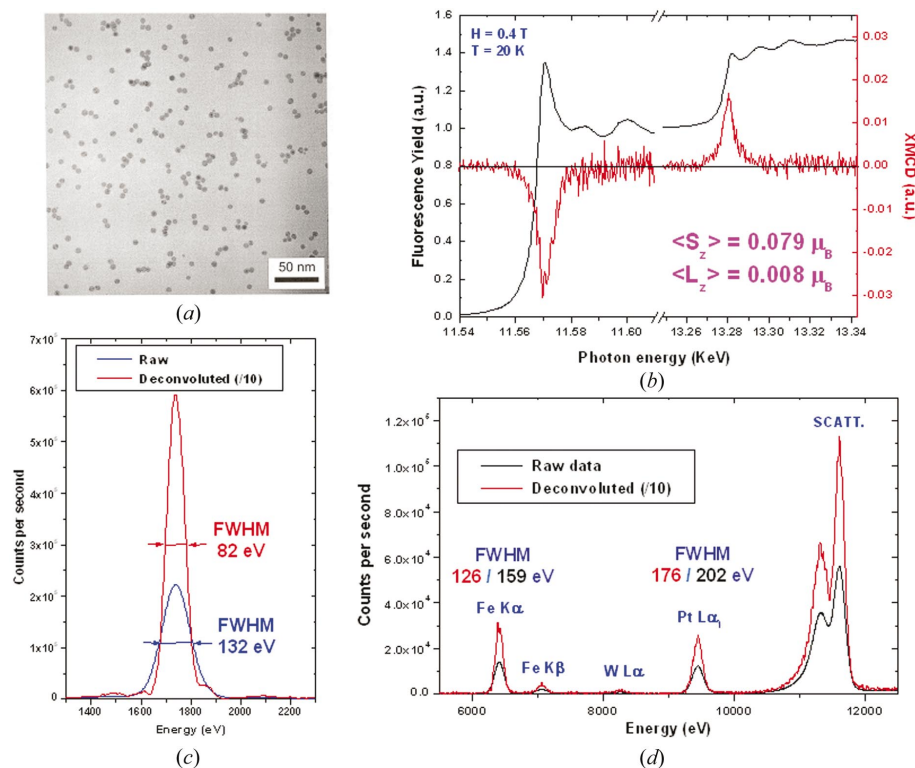
Figure 9
Commissioning tests of the 35-element SDD array. (a) TEM image of the $Fe_{70}Pt_{30}$ nanoparticles dispersed on a Si wafer. (b) XANES and XMCD spectra of the $Fe_{70}Pt_{30}$ nanoparticles at the Pt $L_{II–III}$ edges. (c) Raw and deconvoluted emission spectra in the spectral range of the Si $K_{\alpha\beta}$ soft X-ray fluorescence line. (d) Raw and deconvoluted emission spectra in the energy range 6000–12 000 eV.
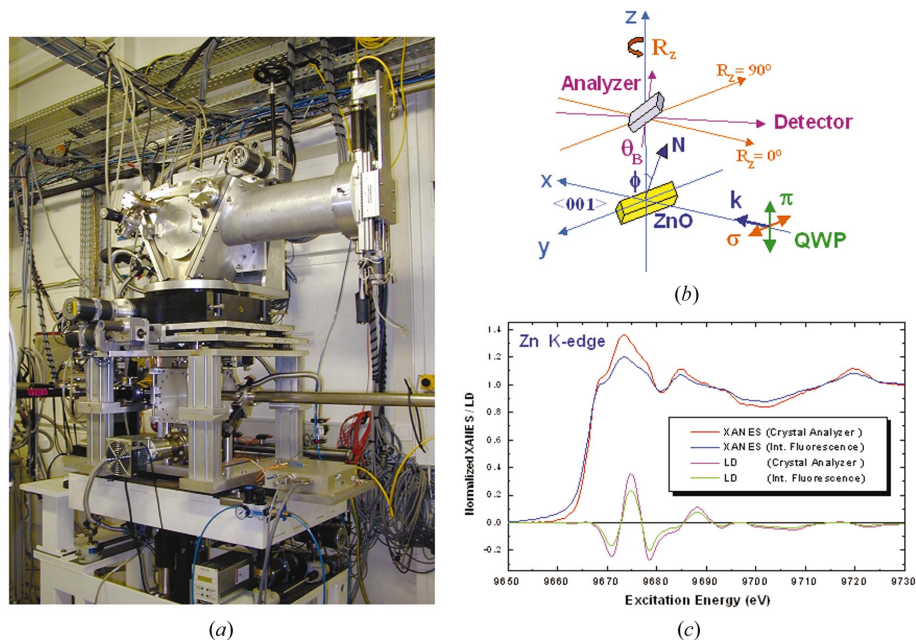
Figure 10
(a) Photograph of the high-vacuum-compatible emission spectrometer. The cube chamber containing the eight-element photodiode arrays can easily be recognized. (b) Block diagram illustrating the geometry of the linear-dichroism experiments performed with the analyzer. QWP = quarter wave plate. (c) Comparative display of the XANES and X-ray linear dichroism (LD) spectra recorded either with the eight-element photodiode array or the high-resolution analyzer. Note the enhanced intensity of the shape resonances in the XANES spectrum recorded with the analyzer.
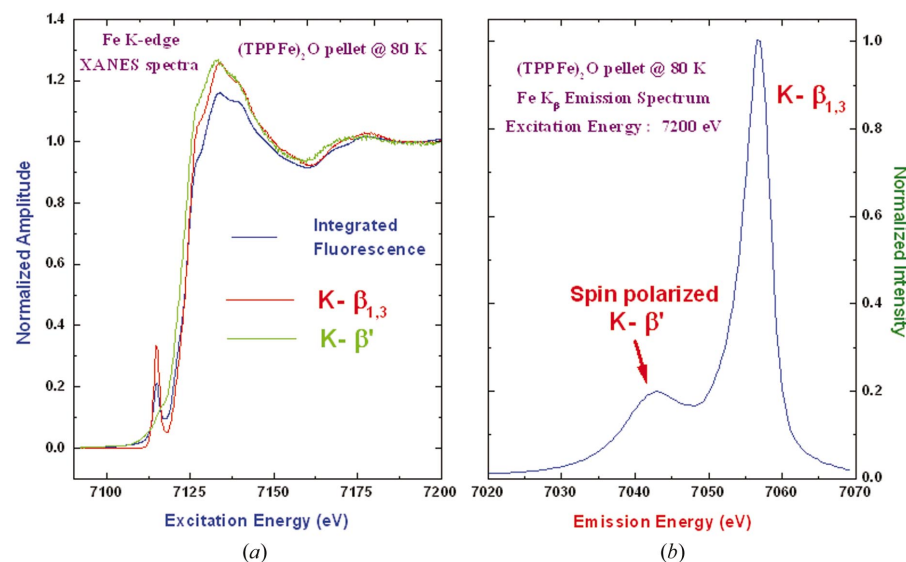
Figure 11
(a) Near-edge X-ray excitation spectra of $[(TPP)Fe]_2O$ recorded by tuning the crystal analyzer to the maximum intensity of either the $K_{\beta1-3}$ fluorescence line or its $K_{\beta'}$ satellite. Note the different intensities and location of the pre-edge structure. The excitation spectrum obtained by recording the total fluorescence yield is also shown for reference. (b) High-resolution emission spectrum of $[(TPP)Fe]_2O$ in the energy range of the $K_{\beta1-3}$ fluorescence line. Note the presence of the spin-polarized $K_{\beta'}$ satellite.

analyzer allowed us to explore the anisotropy of the emission channel around **z**. In the XANES and linear dichroism excitation spectra recorded with the high-resolution analyzer, the near-edge resonances are clearly sharper and enhanced. With our spectrometer we could detect small but significant differences in the linear dichroism spectra when the spectrometer was rotated around the **z** axis, thus confirming the anisotropy of the selected emission channels. The observation of sharper near-edge resonances is a clear indication that what is measured here is a RIXS or resonant Raman process referring to the Kramers–Heisenberg picture of one photon-in/one photon-out. This spectroscopy is a very rich source of additional information on electronic excitations (multiplet states and charge transfer states) in the ground-state configuration (De Groot, 2001). Most remarkable is that, on choosing one particular decay channel, one could partly remove the core-hole lifetime broadening in XANES spectra (Hämäläinen et al., 1991).

Particularly noteworthy is also the investigation of the well resolved $K_{\beta'}$ satellite of the $K_{\beta1-3}$ line in high-spin iron or manganese compounds. This is because it was suggested that the $K_{\beta'}$ satellite could result from a spin polarization of the 3p electrons by exchange correlation with the valence 3d electrons (Hämäläinen et al., 1992). If this interpretation could be firmly established, one could have access to spin-selective XANES or even EXAFS spectra (Wang & Cramer, 1997; De Groot, 2001). As a matter of illustration, we have reproduced in Fig. 11(b) the high-resolution emission spectrum of the μ-oxo di-iron tetraphenyl porphyrinato complex $[(TPP)Fe]_2O$ recorded with a Si (531) spherically bent analyzer at an excitation energy of 7146 eV. The measured energy resolution was then of the order of 1 eV. The RIXS excitation spectra recorded on tuning the analyzer either at the maximum of the $K_{\beta1-3}$ line or at the maximum of the weaker $K_{\beta'}$ satellite are shown in Fig. 11(a), together with the 'integrated fluorescence' XANES spectrum recorded with our eight-element photodiode array. As expected, the differences are most spectacular in the pre-edge region where

photons along the **z** direction. With a bent Si(440) single crystal, the Bragg angle was ∼48.4° at the zinc absorption K edge (9666 eV), the energy resolution being then of the order of 6 eV. At such a Bragg angle, the analyzer itself acts as a polarimeter mostly selecting the polarization component normal to the diffraction plane: thus a rotation R_z of the whole

transitions to bound states take place. Again we note the strong enhancement and sharper pre-peak in the spectrum recorded at the maximum of the $K_{\beta1-3}$ line, whereas this structure is shifted towards higher energy for the spectrum recorded with the $K_{\beta'}$ satellite and appears only as a weak shoulder. Significant differences were recorded in the corresponding EXAFS spectra as well. Finally, we wish to recall that there is abundant literature suggesting that the chemical shifts of the K_β lines could be correlated with the charge and apparent oxidation state of the absorbing atom: accurate measurements of the chemical shifts could therefore be exploited as useful complements to XANES studies, especially in BioXAS.

Unfortunately, even at third-generation synchrotron radiation facilities the count rates still remain rather poor for dilute samples (≤ 30 kcounts s^{-1}). This is particularly critical for polarization-dependent measurements with Bragg angles of the order of 45° because sagittal focusing is ineffective. As a consequence, the focal spot at the detector location is a narrow line extending typically over at least 80 mm. It is envisaged to replace in the near future the photodiode currently in use by a linear array of Peltier cooled Si drift-diodes operated in the counting mode, with the advantage that one could remove the contamination of the measured signal with some scattering or fluorescence background generated by the spectrometer itself.

5. Conclusions

We have reviewed in this paper three complementary approaches to the detection of X-ray fluorescence excitation spectra. It is our deep conviction that the design of modern beamlines at new third-generation synchrotron radiation facilities should be confronted with quite similar needs and thus, rather similar technical options. Regarding BioXAS, it seems that cheap photodiodes operated in the integrated current mode are most attractive for fast data collection owing to the serious risk of radiation damage: the 'quick gap-scan' technique should be a valuable tool for a number of BioXAS studies on moderately dilute systems. With the recent availability of high-resolution crystal analyzers, one can now access additional information by recording valence- or spin-selective XANES or EXAFS spectra in the photon-in/photon-out RIXS mode. Regarding BioXAS, there is again a major risk of radiation damage of fragile samples exposed to a very intense focused beam for very long data-acquisition times since the measured count rates are rather low. There is unfortunately only a fairly limited possibility of increasing the angular acceptance of such instruments without running into the enormous complication of multi-crystal analyzers.

Si drift-diodes are now becoming commercially available in a wide variety of shapes and sizes which should allow the beamline designers to tailor a detector for a given application and a given sample environment. Large arrays of Si-drift diodes with several hundreds of detection channels should also become sooner or later a reality: such detectors should be most welcome for X-ray holography and BioXAS. Never-

theless, one should realise that the expected gain in count rates (with respect to present systems) will hardly exceed one order of magnitude: this is enormous but still not enough in view of the high fluxes that are already available at third-generation synchrotron radiation sources. On the other hand, such large arrays of Si drift-diodes will have to be operated by highly qualified professional people and a great amount of specialized software will have to be developed in order to come up with useful application-oriented products. This is where interdisciplinary and international collaborations are most desirable, given the huge costs and the desperately long time-scales of such heavy technical developments.

References

Bateman, J. E. (2000). *J. Synchrotron Rad.* **7**, 307–312.

Bergonzo, P., Brambilla, A., Tromson, D., Marshall, R. D., Jany, C., Foulon, F., Gauthier, C., Solé, V. A., Rogalev, A. & Goulon, J. (1999). *J. Synchrotron Rad.* **6**, 1–5.

Bertuccio, G., Castoldi, A., Longoni, A., Sampietro, M. & Gauthier, Ch. (1992). *Nucl. Instrum. Methods A*, **312**, 613–616.

Bertuccio, G., Gatti, E., Sampietro, M., Rehak, P. & Rescia, S. (1992). *Nucl. Instrum. Methods A*, **322**, 271–279.

Bordessoule, M. & Bosshard, R. (1995). *Nucl. Instrum. Methods A*, **356**, 452–456.

Carra, P., Thole, B. T., Altarelli, M. & Wang, X. D. (1993). *Phys. Rev. Lett.* **70**, 694–697.

Farrow, R. C., Headspith, J., Dent, A. J., Dobson, B. R., Bilsborrow, R. L., Ramsdale, C. A., Stephenson, P. C., Brierley, S., Derbyshire, G. E., Sangsinkeow, P. & Buxton, K. (1998). *J. Synchrotron Rad.* **5**, 845–847.

Gatti, E. & Rehak, P. (1984). *Nucl. Instrum. Methods A*, **225**, 608–614.

Gaudry, E., Kiratisin, A., Sainctavit, P., Brouder, C., Mauri, F., Ramos, A., Rogalev, A. & Goulon, J. (2003). *Phys. Rev. B*, **67**, 129702.

Gauthier, Ch. (1992). PhD thesis, Université H. Poincaré, Nancy-I, France.

Gauthier, C., Goujon, G., Feite, S., Moguiline, E., Braicovich, L., Brookes, N. B. & Goulon, J. (1995). *Physica B*, **208/209**, 232–234.

Gauthier, C., Goujon, G., Goulon, J., Moguiline, E., Dressler, P., Henck, R. & Lampert, M.-O. (1998). *J. Synchrotron Rad.* **5**, 863–865.

Gauthier, Ch., Goulon, J., Moguiline, E., Elleaume, P., Feite, S., Gaburro, Z., Longoni, A., Gatti, E., Dressler, P., Lampert, M.-O. & Henck, R. (1994). *Nucl. Instrum. Methods A*, **349**, 258–262.

Gauthier, Ch., Goulon, J., Moguiline, E., Fiorini, C., Longoni, A., Sampietro, M., Lechner, P., Strüder, L. & Walenta, A. H. (1997). *J. Phys. IV (France)*, **7**(C2), 337–338.

Gauthier, Ch., Goulon, J., Moguiline, E., Rogalev, A., Lechner, P., Strüder, L., Fiorini, C., Longoni, A., Sampietro, M., Besch, H., Pfitzner, R., Schenk, H., Tafelmeier, U., Walenta, A., Misakos, K., Kavadias, S. & Loukas, D. (1996). *Nucl. Instrum. Methods A*, **382**, 524–532.

Gauthier, Ch., Solé, V. A., Signorato, R., Goulon, J. & Moguiline, E. (1999). *J. Synchrotron Rad.* **6**, 164–166.

Georgiev, A. & Gast, W. (1993). *IEEE Trans. Nucl. Sci.* NS-**40**, 770–779.

Goujon, G., Gauthier, Ch., Moguiline, E. & Goulon, J. (1998). *Proceedings of the 8th European Symposium on Semiconductor Detectors*, Schloss Elmau, Germany.

Goulon, J. (1991). *Proceedings of the European Workshop on X-ray Detectors for SR Sources*, Aussois, France, edited by A. H. Walenta, pp. 39–50.

Goulon, J., Goulon-Ginet, C., Cortès, R. & Dubois, J. M. (1982). *J. Phys. (Paris)*, **43**, 539–548.

Goulon, J., Goulon-Ginet, C., Rogalev, A., Benayoun, G., Malgrange, C. & Brouder, C. (1999). *Proc. SPIE*, **3773**, 316–325.

Goulon, J., Rogalev, A., Gauthier, Ch., Goulon-Ginet, Ch., Pasté, S., Signorato, R., Neuman, C., Varga, C. & Malgrange, C. (1998). *J. Synchroton Rad.* **5**, 232–238.

Groot, F. de (2001). *Chem. Rev.* **101**, 1779–1808.

Guazzoni, C., Sampietro, M. & Fazzi, A. (2000). *Nucl. Instrum. Methods A*, **443**, 447–450.

Hämäläinen, K., Kao, C. C., Hastings, J. B., Siddons, D. P., Berman, L. E., Stojanoff, V. & Cramer, S. P. (1992). *Phys. Rev. B*, **46**, 14274–14277.

Hämäläinen, K., Siddons, D. P., Hastings, J. B. & Berman, L. E. (1991). *Phys. Rev. Lett.* **67**, 2850–2853.

Iwanczyk, J. S., Patt, B. E., Tull, C. R., Segal, J. D., Kenney, C. J., Bradley, J., Hedman, B. & Hodgson, K. O. (1999). *IEEE Trans. Nucl. Sci.* **46**, 284–288.

Iwanczyk, J. S., Patt, B. E., Vilkelis, J., Rhen, L., Metz, B., Hedman, B. & Hodgson, K. O. (1996). *Nucl. Instrum. Methods A*, **380**, 288–294.

Jordanov, V. T. & Knoll, G. F. (1994). *Nucl. Instrum. Methods A*, **345**, 337–345.

Kemmer, J., Lutz, G., Prechtel, U., Schuster, K., Sterzik, M., Strüder, L. & Ziemann, T. (1990). *Nucl. Instrum. Methods A*, **288**, 92–98.

Knoll, G. F. (1989). *Radiation Detection and Measurements.* New York: John Wiley.

Labanti, C., Fiorini, C., Longoni, A., Mauri, A., Perotti, F. & Rossi, E. (2000). *Proceedings of the IEEE Nuclear Sciences Symposium and Medical Imaging Conference*, Lyon, France. Paper 283.

Lechner, P., Fiorini, C., Hartmann, R., Kemmer, J., Krause, N., Leutenegger, P., Longoni, A., Soltau, H., Stötter, D., Stötter, R., Strüder, L. & Weber, U. (2001). *Nucl. Instrum. Methods A*, **458**, 281–287.

Longoni, A., Fiorini, C., Guazzoni, C., Gianoncelli, A., Strüder, L., Soltau, H., Lechner, P., Bjeomikhov, A., Schmalz, J., Langhoff, N. & Wedell, R. (2002). *IEEE Trans. Nucl. Sci.* **49**, 1001–1006.

Matsushita, T. & Hashizume, H. (1983). *Handbook of Synchrotron Radiation*, Vol. 1, edited by E. E. Koch, pp. 261–314. Amsterdam: North-Holland.

Matsuura, H. & Nishida, K. (1998). *Jpn. J. Appl. Phys.* **37**, L115–L118.

Moguiline, E. (1996). PhD thesis, Université J. Fourier, Grenoble-I, France.

Moguiline, E., Gauthier, C., Goujon, G., Goulon, J., Lampert, M.-O., Dressler, P. & Henck, R. (1997). *J. Phys. (Paris) IV*, **7**(C2), 339–340.

Nashashibi, T. & White, G. (1990). *IEEE Trans. Nucl. Sci.* **37**, 452–456.

Pietraski, P. J. & Furenlid, L. R. (2000). *Proceedings of the IEEE Nuclear Sciences Symposium and Medical Imaging Conference*, Lyon, France. Paper 592.

Pietraski, P. J., Voltz, P. & Furenlid, L. R. (1999). *J. Synchrotron Rad.* **6**, 152–154.

Pinotti, E. (1993). PhD thesis, Politecnico di Milano, Italy.

Pinotti, E., Bräuninger, H., Findeis, N., Gorke, H., Hauff, D., Holl, P., Kemmer, J., Lechner, P., Lutz, G., Kink, W., Meidinger, N., Metzner, G., Predehl, P., Reppin, C., Strüder, L., Trumper, J. & von Zanthier, C. (1993). *Nucl. Instrum. Methods A*, **326**, 85–91.

Pullia, A., Fiorini, C. & Gatti, E. (1998). *IEEE Trans. Nucl. Sci.* **45**, 3179–3183.

Pullia, A., Fiorini, C., Gatti, E., Longoni, A. & Buttler, W. (2000). *Nucl. Instrum. Methods A*, **439**, 385–390.

Pullia, A., Geraci, A. & Ripamonti, G. (2000). *Nucl. Instrum. Methods A*, **439**, 378–384.

Radeka, V., Rehak, P., Rescia, S., Gatti, E., Longoni, A., Sampietro, M., Bertuccio, G., Holl, P., Strüder, L. & Kemmer, J. (1989). *IEEE Electron Device Lett.* **10**, 91–94.

Retournard, A., Loos, M., Ascone, I., Goulon, J., Lemonnier, M. & Cortès, R. (1986). *J. Phys.* **47**, C8-143–147.

Ripamonti, G. & Pullia, A. (1996). *Nucl. Instrum. Methods A*, **382**, 545–547.

Rogalev, A., Gotte, V., Goulon, J., Gauthier, C., Chavanne, J. & Elleaume, P. (1998). *J. Synchrotron Rad.* **5**, 989–991.

Rogalev, A., Goulon, J., Goulon-Ginet, Ch. & Malgrange, C. (2001). *Instrumentation Developments for Polarization Dependent X-ray Spectroscopies*, in *Magnetism and Synchrotron Radiation, Springer Lecture Notes in Physics 565*, edited by E. Beaurepaire, F. Scheurer, G. Krill and J.-P. Kappler, pp. 60–86. Berlin: Springer.

Sampietro, M., Bertuccio, G., Geraci, A. & Fazzi, A. (1995). *Rev. Sci. Instrum.* **66**, 975–981.

Sampietro, M., Geraci, A., Fazzi, A. & Lechner, P. (1995). *Rev. Sci. Instrum.* **66**, 5381–5382.

Sampietro, M., Fasoli, L., Gatti, E., Guazzoni, C., Fazzi, A., Lechner, P., Kemmer, J., Hauf, D. & Strüder, L. (2000). *Nucl. Instrum. Methods A*, **439**, 368–372.

Sampietro, M., Fasoli, L., Rehak, P. & Strüder, L. (1995). *IEEE Trans. Electron Devices*, **16**, 142–147.

Solé, V. A., Gauthier, Ch., Goulon, J. & Natali, F. (1999). *J. Synchrotron Rad.* **6**, 174–175.

Sonsky, J., Koornneef, R., Huizenga, J., Nanver, L., Lubking, G. W., Hollander, R. W. & van Eijk, C. W. E. (2000). *Proceedings of the IEEE Nuclear Sciences Symposium and Medical Imaging Conference*, Lyon, France. Paper 362.

Stein, J., Scheuer, F., Gast, W. & Georgiev, A. (1996). *Nucl. Instrum. Methods B*, **113**, 141–145.

Strüder, L., Eckbauer, S., Hartmann, R., Hauff, D., Holl, P., Kemmer, J., Lechner, P., Meidinger, N., Richter, R., Soltau, H., von Zanthier, C., Fiorini, C., Longoni, A. & Sampietro, M. (1997). *J. Phys. (Paris) IV*, **7**(C2), 21–29.

Strüder, L., Fiorini, C., Gatti, E., Hartman, R., Holl, P., Krause, N., Lechner, P., Longoni, A., Lutz, G., Kemmer, J., Meidinger, N., Popp, M., Soltau, H., Weber, U. & von Zanthier, C. (1998). *J. Synchrotron Rad.* **5**, 268–274.

Thole, B. T., Carra, P., Sette, F. & van der Laan, G. (1992). *Phys. Rev. Lett.* **68**, 1943–1946.

Wang, X. & Cramer, S. P. (1997). *J. Phys. IV (France)*, **7**(C2), 361–363.

Zhang, K., Rosenbaum, G. & Bunker, G. (1998). *J. Synchrotron Rad.* **5**, 1227–1234.

Zhang, K., Rosenbaum, G. & Bunker, G. (1999). *J. Synchrotron Rad.* **6**, 220–224.

Zhong, Z., Chapman, D., Bunker, B., Bunker, G., Fischetti, R. & Segre, C. (1999). *J. Synchrotron Rad.* **6**, 212–214.